

Scalable and accurate multi-GPU based image reconstruction of large-scale ptychography data

Xiaodong Yu^{1,*}, Viktor Nikitin², Daniel J. Ching², Selin Aslan², Doğa Gürsoy^{2,3}, and Tekin Bicer^{1,2,*}

¹Data Science and Learning Division, Argonne National Laboratory, 9700 Cass Avenue, Lemont, Illinois 60439, USA

²X-ray Science Division, Argonne National Laboratory, 9700 Cass Avenue, Lemont, Illinois 60439, USA

³Department of Electrical Engineering and Computer Science, Northwestern University, 2145 Sheridan Road, Evanston, Illinois 60208, USA

*{xyu, tbicer}@anl.gov

ABSTRACT

While the advances in synchrotron light sources, together with the development of focusing optics and detectors, allow nanoscale ptychographic imaging of materials and biological specimens, the corresponding experiments can yield terabyte-scale large volumes of data that can impose a heavy burden on the computing platform. While Graphical Processing Units (GPUs) provide high performance for such large-scale ptychography datasets, a single GPU is typically insufficient for analysis and reconstruction. Several existing works have considered leveraging multiple GPUs to accelerate the ptychographic reconstruction. However, they utilize only Message Passing Interface (MPI) to handle the communications between GPUs. It poses inefficiency for the configuration that has multiple GPUs in a single node, especially while processing a single large projection, since it provides no optimizations to handle the heterogeneous GPU interconnections containing both low-speed links, e.g., PCIe, and high-speed links, e.g., NVLink. In this paper, we provide a multi-GPU implementation that can effectively solve large-scale ptychographic reconstruction problem with optimized performance on intra-node multi-GPU. We focus on the conventional maximum-likelihood reconstruction problem using conjugate-gradient (CG) for the solution and propose a novel hybrid parallelization model to address the performance bottlenecks in CG solver. Accordingly, we develop a tool called PtyGer (**P**tychographic **G**PU(**m**ultiple)-based reconstruction), implementing our hybrid parallelization model design. The comprehensive evaluation verifies that PtyGer can fully preserve the original algorithm's accuracy while achieving outstanding intra-node GPU scalability.

Introduction

Coherent diffraction imaging (CDI) is a lensless technique that can produce nanometer-scale resolution images by avoiding lens-imposed limitations of the traditional microscopy¹⁻⁶. Ptychography⁷ is a scanning CDI technique that has gained popularity due to the increasing brilliance and coherence of the synchrotron light sources⁸. Ptychography benefits from the advantages of both CDI and the scanning-probe microscopy by using a focused beam of light (a.k.a the probe) to scan the object at a series of overlapping scan positions, and collecting the corresponding diffraction patterns at the far-field by a pixelated detector. It can be extended to 3D by rotating the object to different view angles and repeating the scanning process at each view to yield a tomographic dataset⁹ or by using the new acquisition methods that are based on rotation as the “fast” scan-axis¹⁰. A range of image reconstruction models and iterative solution methods¹¹⁻¹⁸ has been proposed to reconstruct the object based on the solutions of the phase-retrieval problem. Because the data volume is high that can reach to terabytes, all these approaches are compute-intensive and can require a significant amount of time when running on a single processing unit, either CPU or GPU¹⁹.

Over the last decade, Graphics Processing Units (GPUs) have been broadly used for general-purpose computing due to their massive parallelism and computational power. The applications from various domains have been successfully accelerated with GPUs, including network intrusion detection²⁰⁻²³, biological sequence alignment^{24,25}, program analysis^{26,27}, and tomographic reconstruction²⁸⁻³², to name a few. Several existing works^{33,34} have implemented the standard algorithms for ptychographic reconstruction on a single GPU. However, still the memory of a GPU falls in short compared to the data volumes of even a single view produced by ptychography experiments (see Sec. Reconstruction efficiency). Furthermore, the upcoming upgrade of the light source facilities will provide up to two orders of magnitude improvement in beam brightness, which will lead to a proportional increase in ptychography dataset sizes. These challenges motivate us to leverage multiple GPU devices, and therefore utilize aggregated memory, to parallelize and accelerate ptychographic reconstruction.

Most of the current state-of-the-art high-performance computing systems are configured as multi-node multi-GPU ma-

chines^{35–37}. Accelerating applications on these machines demand proper synchronizations and communications among the GPU devices. A few existing works^{19,38,39} implement ptychography on multi-GPU with various reconstruction algorithms including ePIE¹³, relaxed averaged alternating reflections (RAAR)⁴⁰, and difference map (DM)¹⁴. However, they all utilize only Message Passing Interface (MPI) to handle the communications. MPI⁴¹, the *de facto* standard of inter-node communication handling, has been well established, and its functionality has been extended to be GPU-aware^{42–44}. However, it has sub-optimal performance for intra-node GPU-GPU communications due to the factors such as the heavy overhead for shared memory model and the under-utilization of the high-speed low-speed mixed links. Recently, NVIDIA has proposed NVIDIA Collective Communications Library (NCCL)⁴⁵ for multi-GPU communications. It provides lightweight and optimized multi-threading solutions for handling intra-node GPU-GPU communications. Coupling NCCL with MPI can offer optimal performances for multi-GPU computing that requires both inter-node and intra-node communications.

In this paper, we introduce a parallelization design for solving the maximum-likelihood (ML) ptychographic reconstruction problem using a conjugate-gradient (CG) solver³³ on multi-GPU systems. Our design incorporates multi-threading GPU-GPU communications to enable reconstruction of large views with aggregated GPU memories. CG solver is known to converge faster than the gradient descent based approaches (such as parallel ePIE) and is fully scalable. However, implementation of CG on multi-GPU exposes challenges in preserving the full algorithmic equivalence because of the required scatter-gather operations (see Sec. Challenges of CG solver parallelization). Towards this end, our work proposes a novel parallelization model to fit the multi-GPU CG solver. In our model, we split each reconstruction iteration into four stages and then apply different communication patterns to different stages to accomplish various data transfer requests. This advanced design maintains the full equivalence of the original CG solver and minimizes the multi-GPU implementation overhead. Subsequently, we implemented our solution in the **Ptychographic GPU(multiple)-based reconstruction** that we call PtyGer, an openly available software package. Our experiments demonstrate that PtyGer can provide reconstructions with remarkable multi-GPU scalability while maintaining the accuracy of the solution. In addition, PtyGer can be easily extended to 3D ptychography thanks to the data independence between the view angles and the tomo-ptycho joint solvers⁹. PtyGer also provides interfaces for other scalable algorithms that follows a similar data processing pattern^{14,15,46} to be plugged into. Our contributions can be summarized as follows:

- We propose a fine-grained parallelization design for ptychographic reconstruction on multiple GPUs. We explore the challenges of parallelizing the conjugate-gradient solver based maximum-likelihood phase-retrieval algorithm, and accordingly provide a novel hybrid model to tackle the challenges.
- We develop a ptychographic reconstruction software called PtyGer. PtyGer implements our hybrid model design using Python and CUDA. It is scalable in terms of both dataset volume and GPU configuration.
- We extensively evaluate the efficacy and efficiency of PtyGer. We use both synthetic and real-world experimental dataset with various data volumes. The results show that PtyGer can provide accurate reconstruction with outstanding multi-GPU scalability.

Related work

A variety of ptychographic reconstruction algorithms have been proposed during the past two decades. The ptychographic iterative engine (PIE)^{11,12} is an iterative phase-retrieval approach employing the diffraction patterns as a known illumination function. It demonstrates fast convergence rate^{47,48}. However, it lacks the robustness when noise is present in measurements. Moreover, the PIE and its variants (ePIE^{13,49}, 3PIE⁵⁰) are inherently sequential since they have to update probe and object images after processing each diffraction pattern. In contrast to the PIE family, some reconstruction algorithms are parallelizable⁵¹, including the difference map (DM) algorithm^{14,15} and the relaxed averaged alternating reflections (RAAR) algorithm⁴⁰. Another notable parallel-friendly ptychographic reconstruction approach uses the maximum-likelihood (ML) model^{17,18} and is derived from the cost-function optimization technique¹⁶. The DM and RAAR algorithms and ML-based models that use CG solver are all naturally parallelizable since they only need to update the estimated object image after simultaneously processing a set of diffraction patterns. Recently, some advanced techniques^{9,52} have been proposed to further refine the reconstructed images.

There are several existing works that discuss the GPU-based implementations of ptychography. PyNX⁵³ implements the DM algorithm on the GPU using OpenCL language. PtychoShelves³⁴ provides a MATLAB-based GPU reconstruction engine that supports the DM and ML algorithms. However, both of them only allow reconstructions on a single GPU. Marchesini et al. developed a multi-GPU-based ptychographic solver called SHARP³⁹ implementing the RAAR algorithm. Dong et al. implemented the DM algorithm on multiple GPUs¹⁹. But they utilize only MPI to handle both intra- and inter-node multi-GPU processing, and thus are sub-optimal. Although CUDA-aware MPI enables direct GPU-GPU data access and transfer, MPI is not optimized for the intra-node multi-GPU communications due to inefficient utilization of high-speed links, e.g., NVLink. PtychoLib³⁸ proposes a fine-grained design for the multi-GPU based ptychography. It parallelizes the ePIE by simultaneously

processing all diffraction patterns and updating the reconstructed image only once in each iteration. However, this parallelization does not comply with the design principle of ePIE and can introduce artifacts while reconstructing experimental data. Besides, it also suffers from the sub-optimal performance of MPI for intra-node GPU-GPU communications.

The difficulty of scaling applications on multi-GPU configurations is often underestimated. Simply distributing the workloads and duplicating the single-GPU procedure onto other GPUs usually lead to incorrect results and poor scaling. Therefore, implementations on multi-GPU configurations require design considerations for communications via mixed topology containing both PCIe and NVlink, asynchronous execution-communication, and so on. There are limited number of studies that focus on designing fine-grained multi-GPU based implementations. BLASX⁵⁴ is a library providing high-performance Level-3 BLAS primitives for the multi-GPU based linear algebra. Gunrock⁵⁵ and Groute⁵⁶ are two frameworks that support the multi-GPU graph analytics. MAPS-Multi⁵⁷ and Blink⁵⁸ propose the designs for the multi-GPU based machine learning. All these works optimize multi-GPU performance by carefully balancing application workload and tuning GPU P2P communication while considering both algorithmic and multi-GPU architectural characteristics. They verify that the fine-grained parallelization is essential to fully unleash the multi-GPU's computing power for accelerating real-world applications.

Results and Discussions

We evaluate both the efficacy and efficiency of our CG-solver based PtyGer (**P**tychographic **G**PU(multiple)-based **r**econstruction) tool on a multi-GPU platform. This platform equips two Intel Xeon Silver 4116 CPUs (host) and eight NVIDIA GeForce RTX 2080Ti GPUs (devices). The host has 768GB total memory and each CPU consists of 12 physical cores (or 24 cores in total for a host). Each 2080Ti card is built upon the latest Turing micro-architecture and integrates 68 streaming multiprocessors (SM) with 64 CUDA cores per SM, hence totally holds 4352 CUDA cores on chip. Each card has a 11GB off-chip global memory that is shared by all SMs. All 68 SMs also share a 5.5MB on-chip L2 cache, and each SM has a 64KB private L1 cache (shared memory). The GPUs are interconnected using PCIe that are capable of 11GB/s unidirectional bandwidth. The Turing micro-architecture disables P2P communication via PCIe, hence the GPU-GPU data transfers are accomplished via host memory.

We evaluate our tool using three dataset: *siemens-star*, *coins*, and *pillar*. The first two dataset are synthetic produced by generating the diffraction patterns from a test image (*siemens-star*) and a real image (*coins*), respectively. The third dataset is a real experimental data from an integrated circuit (IC) sample, and collected at 2-ID-D microscopy beamline at Advanced Photon Source with $0.2\ \mu\text{m} \times 0.2\ \mu\text{m}$ beam size (<https://www.aps.anl.gov/Microscopy/Beamlines/2-ID-D>). The dimensions of the reconstructed images are 2048×2048 , 1024×1024 , and 1024×768 , respectively. The probe dimensions are 256×256 for all dataset. We introduce different computation demands for reconstructions by sub-sampling each of the dataset to 4K, 8K, and 16K diffraction patterns. The total number of iterations is set to 128 for all reconstructions.

Reconstruction efficacy

In this section, we evaluate the efficacy of PtyGer by examining the accuracy of the reconstructions. For each dataset, we calculate the structural similarity (SSIM)⁵⁹ and peak signal-to-noise ratio (PSNR) between the reconstructed image and the reference image (ground-truth) after each iteration. 1 in SSIM indicates perfect structural similarity while a value larger than 50dB in PSNR typically represents that the difference between two images is very tiny. Since the real experimental data have no reference object image, we only evaluate the reconstruction results of synthetic datasets.

Fig. 1 demonstrates the reconstruction accuracy of our PtyGer on *siemens-star* datasets using 8-GPU, 4-GPU, and 2-GPU configurations, respectively. It also includes the single-GPU reconstruction result³³ as the counterpart. In each subfigure, the x-axis indicates the running time of the PtyGer in log-10 scale, while the left-hand y-axis indicates the SSIM and the right-hand y-axis represents PSNR, both between the reconstructed image and the reference image. Fig. 1(a) shows the results on small-scale *siemens-star* dataset (4K diffraction patterns). It indicates that although taking different amount of time, the SSIM of all multi-GPU configurations approach to reference image while the PSNRs start at around 55dB and reach above 80dB at the end. We also observe that the multi-GPU reconstructions have very similar convergence curves compared to the single-GPU based reconstruction. More specifically, after approximate 65 iterations, the multi-GPU based reconstructions have their SSIM and PSNR going beyond 0.95 and 75dB and monotonically increasing towards reference image ever since. Fig. 1(b) and Fig. 1(c) show the results of medium-scale *siemens-star* dataset (8K) and large-scale *siemens-star* dataset (16K), respectively. Similarly, they indicate that multi-GPU based reconstructions on both datasets have their SSIM converging to 1 and PSNR reaching 80dB and expose the same convergence curves compared to their single-GPU based counterparts. Fig. 1(d) compares the actual reconstructed image of the 8K dataset using 4-GPU to the original *siemens-star* image. The zoom-in to the center of the images highlight that the hybrid parallelization model and the sub-image alignment in PtyGer introduce no artifacts. Although reconstructions with different GPU configurations have the same precision, they cost different amount of time to converge. The convergence speed is mainly determined by the per GPU workload that can fit into the GPU memory. For example, while 4K diffraction patterns fit in 2, 4, and 8-GPU configurations, 1-GPU configuration cannot

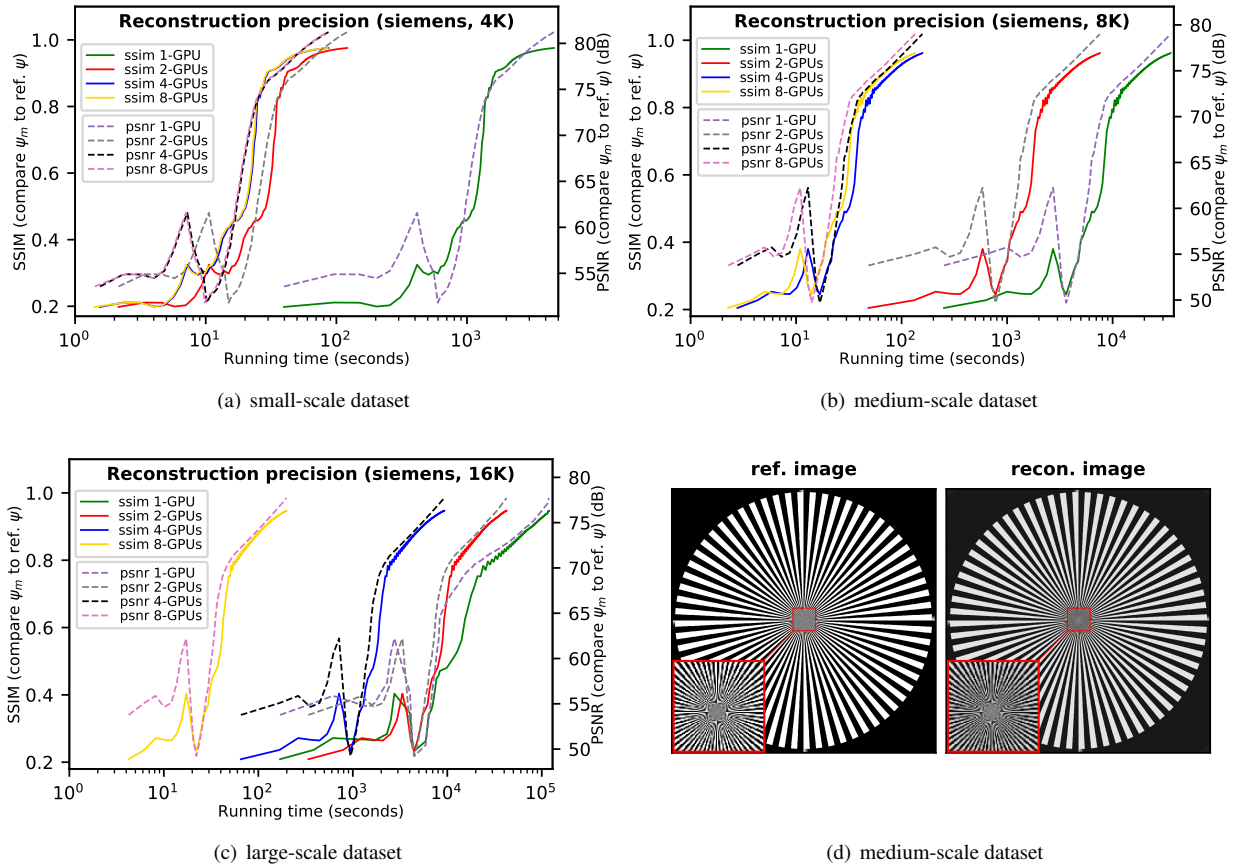


Figure 1. The reconstruction accuracy evaluations using (a) small-scale (4K diffraction patterns), (b) medium-scale (8K), and (c) large-scale (16K) synthetic *siemens-star* datasets. For each evaluation, we calculate both the SSIM and PSNR between the reconstructed image and the reference image after each iteration. We use the running time as the x-axis to distinguish the results of different GPU configurations. It is noteworthy that, in each subfigure, the reconstructions with different number of GPUs actually have the same convergence curve. The visual difference is caused by different speeds of running a iteration. (d) shows the comparison between the 4-GPU reconstructed image of the 8K dataset and the reference image.

accommodate all the data structures and therefore shows significant slowdown compared to other configurations. Similarly, for 16K diffraction patterns, dataset can only fit into 8-GPU configuration, which shows an execution time consistent with 4K diffraction patterns’ dataset. However, all the other configurations show performance degradation due to memory limitations. We will comprehensively evaluate the converging efficiency of PtyGer in next section.

Fig. 2 demonstrates another set of reconstruction accuracy evaluations using the same experimental design as Fig. 1 on small-scale *coins* (Fig. 2(a)), medium-scale *coins* (Fig. 2(b)), and large-scale *coins* (Fig. 2(c)) dataset, respectively. The SSIM and PSNR in Fig. 2 indicate that the reconstructions of *coins* datasets with different multi-GPU configurations all converge to reference image and the convergence curves are identical to their corresponding single-GPU based counterparts’. Fig. 1(d) displays the actual 4-GPU reconstructed image of the 8K dataset and compares it to the original coins image. We note that no artifacts are observed at the zoomed in centers of the images, where the GPUs exchange border information.

Above evaluation results show that our PtyGer tool with various number of GPUs can fully preserve the functional equivalence compared to the original algorithm implemented on a single GPU. The outputs of our multi-GPU based reconstructions are mathematically similar enough to the ground-truths (the reference images), and the convergence trends are identical to the original single-GPU based implementation.

Reconstruction efficiency

In this section, we evaluate our PtyGer’s reconstruction efficiency, i.e., the speedups compared to the single-GPU counterpart³³ (the baseline). Last subsection verifies that our PtyGer preserves the algorithmic equivalence, hence comparing the convergence

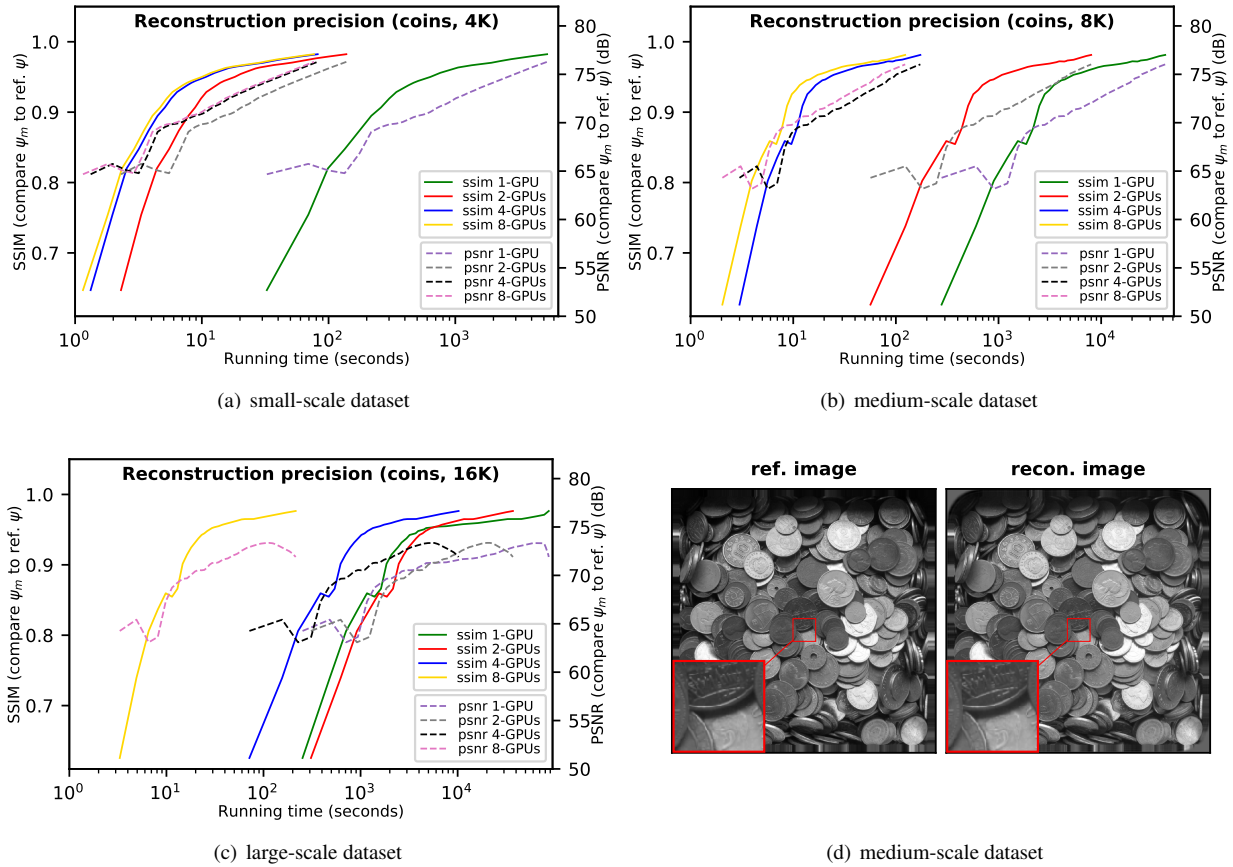


Figure 2. The reconstruction accuracy evaluations using (a) small-scale (4K diffraction patterns), (b) medium-scale (8K), and (c) large-scale (16K) synthetic *coins* datasets. For each evaluation, we calculate both the SSIM and PSNR between the reconstructed image and the reference image after each iteration. We use the running time as the x-axis in order to distinguish the results of different GPU configurations. It is noteworthy that, in each subfigure, the reconstructions with different number of GPUs actually have the same convergence curve. The visual difference is caused by different speeds of running a iteration. (d) shows the comparison between the 4-GPU reconstructed image of the 8K dataset and the reference image.

speeds of the PtyGer to the counterpart can indicate the performance speedups. We measure the convergence speed by recording the least-square norm (2-norm) of the difference between current and previous iterations' outputs (i.e., $\Psi_m - \Psi_{m-1}$). 2-norm being 0 represents perfect convergence. Practically, when the 2-norm goes below a certain threshold, the reconstruction result is considered converged. Notice that our experiments use fixed number of iterations (128) instead of stop criteria, hence the reconstructions keep iterating even if the outputs are converged. Therefore, the 2-norms can decrease further or fluctuate within a small range at the end. We evaluate the PtyGer's efficiency on all nine datasets.

Fig. 3 demonstrates the reconstruction convergence rates of three *siemens-star* datasets using 8, 4, 2 and 1 GPU configurations. In each subfigure, the x-axis indicates the running time and the y-axis indicates the 2-norm. We emphasize that both axes are in log-10 scale. Consequently, the lower bound of 2-norm is negative infinity (i.e., 0 in regular scale). Fig. 3(a) shows the efficiency comparisons of reconstructions on small-scale *siemens-star* dataset (4K diffraction patterns). Fig. 3(b) breaks down the running time under each configuration. We use a broken bar to demonstrate the outlier (i.e., single-GPU). As indicated in both figure, single-GPU based reconstruction takes approximately 1.3 hours. This slow execution is caused by that the size of dataset exceeds the memory capacity of a single GPU. We note that the CG-solver yields large memory footprint during the execution due to buffering the intermediate results. Instead aborting the execution, the reconstruction leverages CUDA unified memory to handle the excess data. It provides the unified virtual address (UVA) space to the GPU and CPU memories, so the program can automatically utilize the CPU memory to assist the GPU execution. However, this technique has a large overhead. As shown in Fig. 3(b), unified memory cost (green segment) dominates the single-GPU execution time (95.8%). The cost

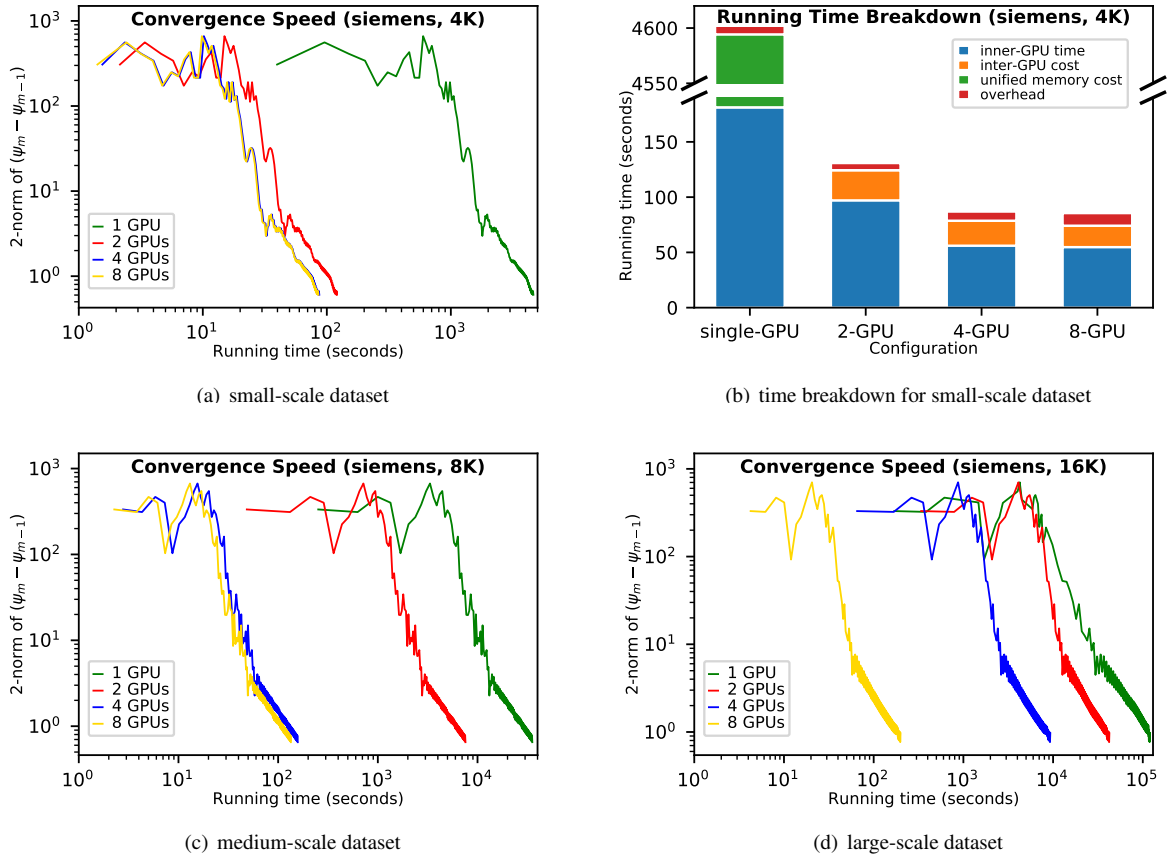


Figure 3. The convergence speed evaluations using (a) small-scale (4K diffraction patterns), (c) medium-scale (8K), and (d) large-scale (16K) synthetic *siemens-star* datasets. For each evaluation, we apply various GPU configurations (single-GPU, 2-GPU, 4-GPU, and 8-GPU), and compute the difference of the reconstructed images before (i.e., ψ_{m-1}) and after (i.e., ψ_m) Update stage in each iteration by measuring pixels’ 2-norm. Notice that we use log-10 scale for both axes. (b) provides more details for (a) by breaking down the running time. In single-GPU, notice that there is no inter-GPU cost and we use a broken bar for unified memory cost for better illustration.

includes expensive CPU-GPU data migrations and page fault handlings occurring at each CUDA arithmetic operation. Fig. 3(a) shows the 2-GPU based reconstruction is 38.6X faster than the original single-GPU reconstruction. The speedup is *superlinear* due to that the splitting of dataset makes the workload of each GPU (2K diffraction patterns per GPU) fit into GPU memory hence the 2-GPU reconstruction avoids host-device communication. Fig. 3(b) shows that inner GPU computing (blue segment) takes the majority (74.2%) of the 2-GPU reconstruction time. One other main component (20.8%) is the inter-GPU cost (orange segment) including GPU-GPU synchronizations and communications. The one-time overhead (red segment) consisting of data preparation and device management is minor (5%). Fig. 3(a) also shows that the 4-GPU based reconstruction has 1.5X speedup compared to the 2-GPU reconstruction. We observe that in Fig. 3(b), although the inner-GPU computing of the 4-GPU is nearly 2X faster due to the halved per GPU workload, the overall speedup is sublinear. The main reason of this is since more number of devices is involved in computation, the inter-GPU cost and one-time overhead are slightly larger than the 2-GPU. Fig. 3(a) shows the 8-GPU based reconstruction has nearly the same efficiency as the 4-GPU configuration. This is because increasing the number of GPUs makes each GPU’s workload (0.5K diffraction patterns) is too small to efficiently occupy the GPU computing resources. Fig. 3(b) shows that both 4-GPU and 8-GPU configurations are memory bound since they have similar computation times.

Fig. 3(c) and 3(d) show the reconstruction efficiency comparisons on medium-scale *siemens-star* dataset and large-scale *siemens-star* dataset, respectively. In Fig. 3(c), we observe that, even though running faster than single-GPU configuration, the 2-GPU reconstruction nevertheless takes very long time since the divided workload on each GPU (4K per GPU) still exceeds the GPU memory capacity. We also observe that the 4-GPU configuration is 42.4X faster than the 2-GPU. The speedup is

superlinear due to the same reason as mentioned before. The 8-GPU based reconstruction is 1.3X faster than the 4-GPU. Compared to the 8-GPU based reconstruction on the small-scale *siemens-star* dataset, the reconstruction on the medium-scale dataset doubles the workload per GPU and therefore better utilizes the computing resources. Thus, for the medium-scale dataset, increasing the GPU number from four to eight can improve the overall performance. Fig. 3(d) shows that, for the large-scale *siemens-star* dataset, even the 4-GPU configuration has insufficient memory. On the other hand, the 8-GPU configuration makes the per GPU workload small enough to fit into the GPU memory and achieves superlinear speedup (41.5X) against the 4-GPU configuration.

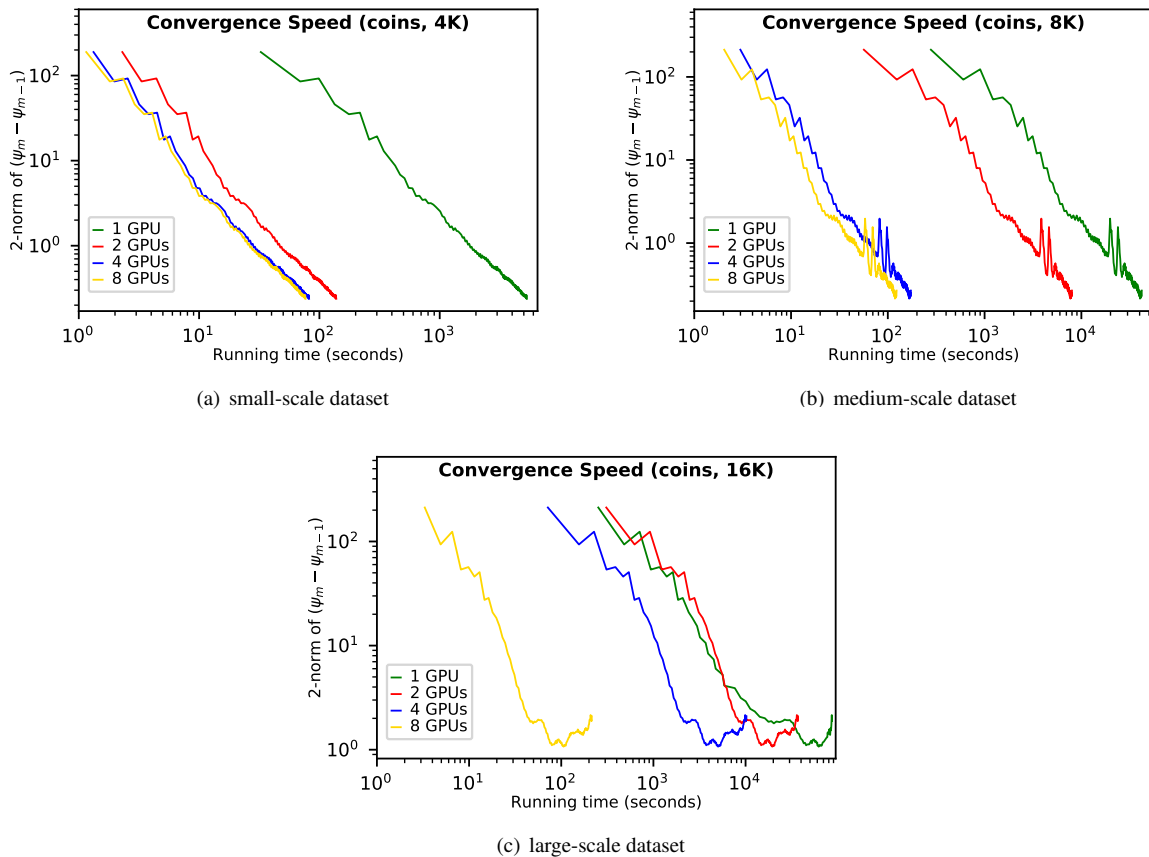


Figure 4. The convergence speed evaluations using (a) small-scale (4K diffraction patterns), (b) medium-scale (8K), and (c) large-scale (16K) synthetic *coins* datasets. For each evaluation, we apply various GPU configurations (single-GPU, 2-GPU, 4-GPU, and 8-GPU), and compute the difference of the reconstructed images before (i.e., ψ_{m-1}) and after (i.e., ψ_m) Update stage in each iteration by measuring pixels' 2-norm. Notice that we use log-10 scale for both axes.

Fig. 4 and Fig. 5 show another two sets of efficiency comparisons on *coins* and *pillar* datasets, respectively. As shown in Fig. 4(a) and Fig. 5(a), for the small-scale datasets, the workloads exceed the capacity of a single GPU memory hence the single-GPU based reconstruction is very slow. The 2-GPU configurations accommodate the per GPU workload within the GPU memory capacity thus achieve superlinear speedups (38.4X in Fig. 4(a) and 39.7X Fig. 5(a) compared to the single-GPU one). Increasing the number of GPUs from two to four can achieve additional 1.7X and 1.6X speedups. However, further increasing the number of GPUs from four to eight shows no improvement due to the underutilized GPU resources. For the medium-scale datasets, the 2-GPU configuration cannot keep the per GPU workload within the GPU memory capacity hence 4-GPU configuration shows 40.2X (Fig. 4(b)) and 42.4X (Fig. 5(b)) superlinear speedups. The 8-GPU configuration can further improve the efficiency by 1.4-fold (Fig. 4(b)) and 1.4-fold (Fig. 5(b)) compared to the 4-GPU. For the large-scale datasets, the per GPU workload exceeds the GPU memory capacity even with four GPUs, but the 8-GPU based reconstructions can still afford the large workloads and achieve superlinear speedups (42.9X (Fig. 4(c)) and 43.1X (Fig. 5(c)), respectively) over the 4-GPU configurations. Fig. 5(d) displays the reconstructed pillar image with 8K diffraction patterns using 4-GPU. Since there is no reference pillar image, we compare the 4-GPU reconstructed image to the single-GPU result. The comparison shows that

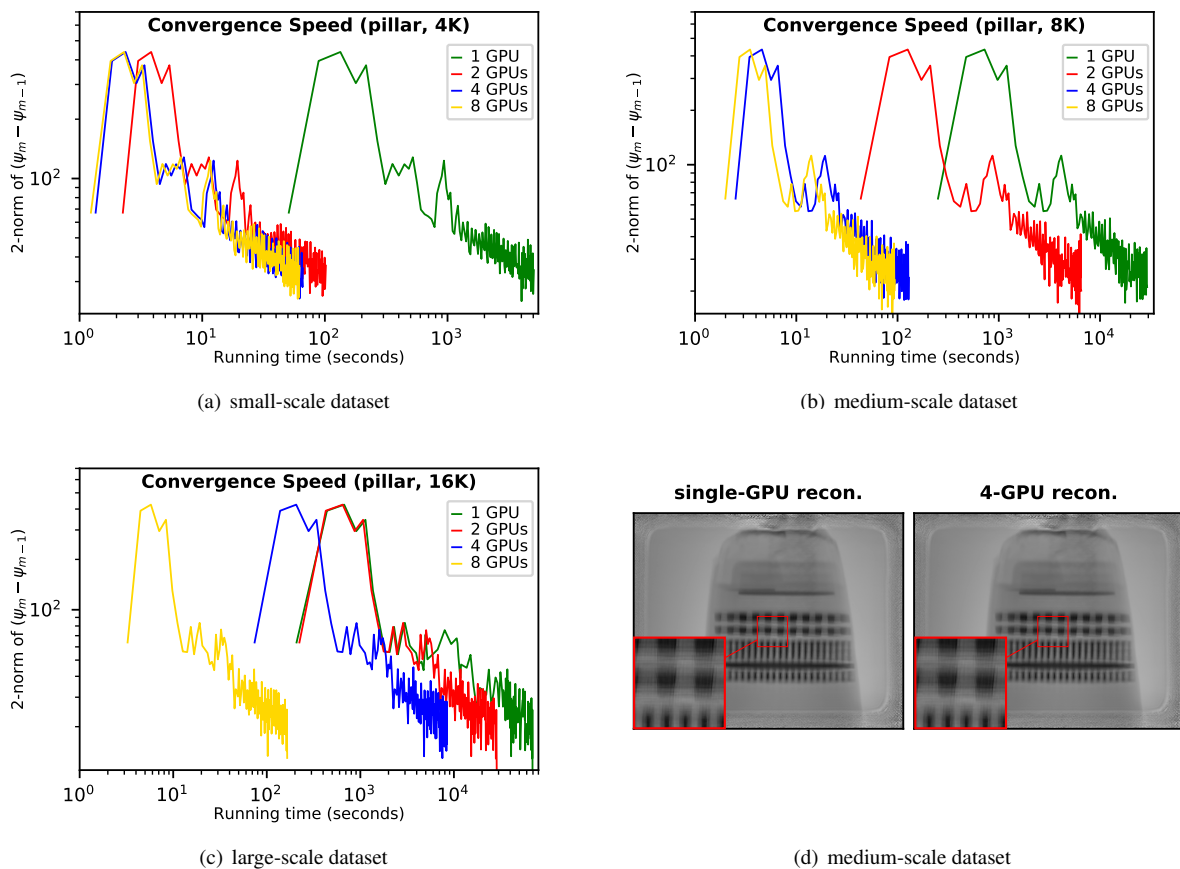


Figure 5. The convergence speed evaluations using (a) small-scale (4K diffraction patterns), (b) medium-scale (8K), and (c) large-scale (16K) real-beamline *pillar* datasets. For each evaluation, we apply various GPU configurations (single-GPU, 2-GPU, 4-GPU, and 8-GPU), and compute the difference of the reconstructed images before (i.e., ψ_{m-1}) and after (i.e., ψ_m) Update stage in each iteration by measuring pixels’ 2-norm. Notice that we use log-10 scale for both axes. (d) compares the 4-GPU reconstructed image of 8K dataset to the single-GPU result.

scaling the reconstruction of real-beamline data to multiple GPUs using PtyGer preserves the reconstructed image’s quality. Focusing on the image centers shows that there are no artifacts at the overlapped regions among GPUs. All above comparisons verify that our multi-GPU PtyGer can successfully increase the overall reconstruction efficiency. The rate of increase is affected by both dataset size and the number of GPU. If the workload exceeds the GPU memory capacity, then adding more number of GPUs can achieve superlinear speedup as aggregated GPUs memory decreases the host-device memory operations. Once the workload fits into aggregated memory, adding more GPUs can still improve the reconstruction efficiency, however the performance improvement is sublinear due to inter-GPU synchronization and communication overheads. However, once the per GPU workload is significantly insufficient to occupy the GPU computing resources, the performance gain stops growing.

Summary and discussion

We comprehensively evaluate our PtyGer using both synthetic and real-beamline data with various sizes. The evaluation of the efficacy shows that PtyGer fully preserves the accuracy of the original sequential algorithm. We also show great scalability efficiency with PtyGer, in some cases superlinear, with increasing number of GPUs and large workloads. The multi-GPU based reconstructions are significantly faster than the single-GPU counterparts due to the elimination of unified memory usage (host-device data movement) and aggregated GPU memory. For the multi-GPU, when the per GPU workload fits into GPU memory, doubling the number of device results in up to 1.7X performance improvement. The sublinearity is caused by the unavoidable preprocessing overhead and inter-GPU costs. Our hybrid parallelization model design has minimized the inter-GPU communication.

The optimal number of GPU devices depends on the dataset size. More GPUs do not necessarily provide better performance.

When the per GPU workload is too small, system reaches the memory I/O bound. Therefore, adding more GPUs will not increase the reconstruction speed and lead to a waste of the computational resources. Empirically, using 2 GPUs for a small dataset can achieve the best resource utilization; 4 GPUs are adequate for a medium dataset; 8 GPUs are needed for a large dataset. Whenever sufficient number of GPUs is utilized for a given workload, any excess GPUs can be used for reconstructing other view angles in 3D ptychography.

Methods

Background

In this section, we provide the background information about the ptychography model, the iterative phase-retrieval algorithm, and the gradient-based solvers.

Forward problem of ptychography

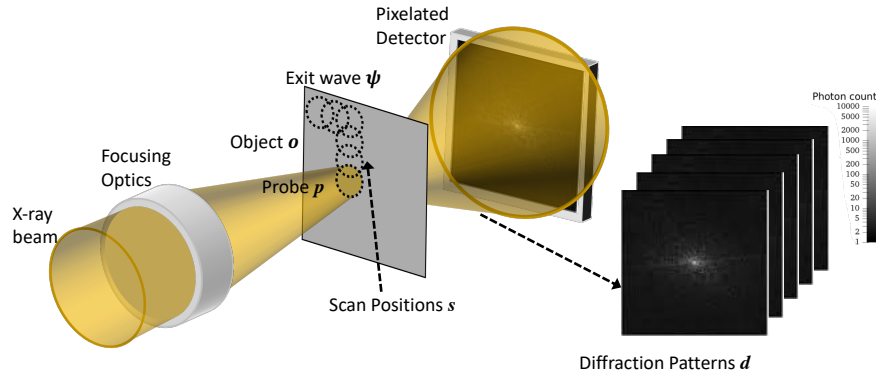


Figure 6. A typical setup of ptychography data collection. The focused probe p raster-scans the object o at overlapped positions s . A series of diffraction patterns of the exit waves are collected by the pixelated detector to form the diffraction data d .

Fig. 6 schematically shows a generic ptychography setup. In ptychography, a focused coherent x-ray beam of light (i.e., probe p) is used to scan the object o , and the diffraction patterns of the transmitted radiation is collected via a pixelated photon counting detector. The probe scans the object in a series of consecutive and overlapped illumination positions (i.e., scan position s in Fig. 6). Accordingly, the detector collects a series of diffraction patterns denoted by d . Ptychography can be mathematically described by the forward model from exit wave ψ to diffraction pattern d :

$$|\mathcal{G}\psi|^2 = |\mathcal{F}\mathcal{Q}\psi|^2 = d, \quad (1)$$

where \mathcal{G} is the ptychography operator that represents applying Fourier transforms \mathcal{F} to the diagonal operator \mathcal{Q} . \mathcal{Q} acts as an element-wise multiplication of probe p and exit wave ψ at all scan positions.

Inverse problem for ptychography

In this section we briefly recapitulate our approach for solving 2D ptychography problem. For details we refer to our former papers^{9,33}, where we considered Maximum-Likelihood (ML) and Least-Squares (LS) estimates for the solution. As an example, here we consider the ML estimate formulation, although all the techniques introduced in this paper are also applicable to the LS estimator.

The exit wave ψ can be numerically reconstructed based on the solution of the phase retrieval problem. Photon collection of the detector is a Poisson process⁶⁰, and the probability of acquiring data d_j , $j = 1, 2, \dots, n$, is given by the likelihood function.

The corresponding maximum likelihood (ML) estimate of ψ then can be computed by solving the following minimization problem

$$F(\psi) = \sum_{j=1}^n \{ |\mathcal{G}\psi|_j^2 - 2d_j \log |\mathcal{G}\psi|_j \} \rightarrow \min, \quad (2)$$

for which the gradient is given as follows

$$\nabla_{\psi} F(\psi) = \mathcal{G}^H \left(\mathcal{G}\psi - \frac{d}{(\mathcal{G}\psi)^*} \right), \quad (3)$$

where $\mathcal{G}^H = \mathcal{Q}^H \mathcal{F}^H$ and \mathcal{Q}^H operates as an element-wise multiplication by the conjugate of probe p , and \mathcal{F}^H is the inverse Fourier transform.

With the gradient, we can iteratively reconstruct the object image using various solvers. We can use the gradient-descent (GD) solver to reconstruct the image⁹. In this case, iterations of updating estimated object can be written as follows

$$\psi_{m+1} = \psi_m - \gamma \nabla_{\psi} F(\psi) \quad (4)$$

where γ is given as a constant small step length. The GD solver has a slower convergence rate compared to conjugate-gradients (CG) family of solvers^{61–64}. In our former work the CG solver with the Dai-Yuan conjugate direction⁶¹ has demonstrated a faster convergence rate in 2D ptychography compared to analogues. The iterations for object updating with the Dai-Yuan direction can be written as:

$$\psi_{m+1} = \psi_m + \gamma_m \eta_m. \quad (5)$$

where γ_m is the step length and η_m is the search direction given by the recursive Dai-Yuan⁶¹ formula:

$$\eta_m = -\nabla_{\psi} F(\psi_m) + \frac{\|\nabla_{\psi} F(\psi_m)\|_2^2}{\langle \eta_{m-1}, \nabla_{\psi} F(\psi_m) - \nabla_{\psi} F(\psi_{m-1}) \rangle} \eta_{m-1} \quad (6)$$

with the initial direction as the steepest descent direction, $\eta_0 = -\nabla_{\psi} F(\psi_0)$. $\langle a, b \rangle$ is defined as $\sum_i^z a_i^* b_i$ and z is the number of pixels of object ψ . The step length γ_m is computed through the line-search procedure⁶⁵. Line-search starts at an initial large step length, and repeatedly shrinks it until the following is satisfied,

$$F(\psi_m + \gamma_m \eta_m) \leq F(\psi_m) + \gamma_m t, \quad (7)$$

where t is a constant termination parameter usually set to 0 in practice.

The complete iterative solution of the ptychographic reconstruction can be summarized with the workflow shown in Fig. 7. In the workflow, an iteration is divided to four stages, where we apply different parallelization schemes to different stages. The details of our parallelization schemes are elaborated in next section.

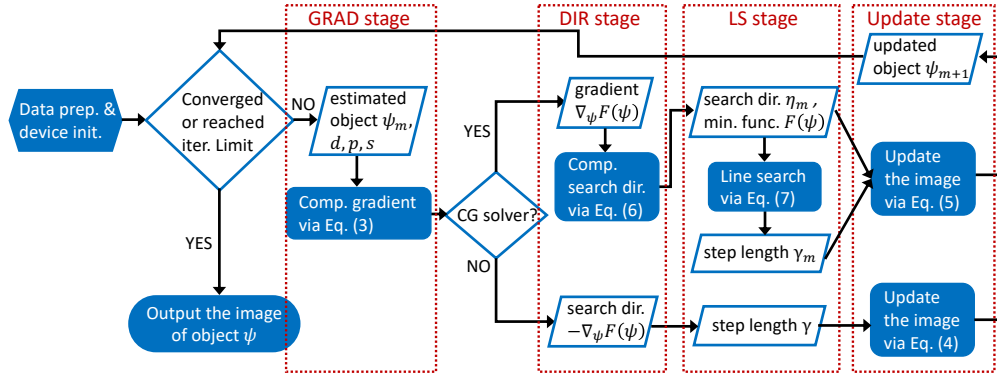


Figure 7. The flowchart of iterative maximum-likelihood phase-retrieval algorithm using the gradient-based solver. Each iteration can be divided into four stages: *GRAD stage*, *DIR stage*, *LS stage*, and *Update stage*.

Multi-GPU based parallelization designs

In this section, we elaborate the design of our novel parallelization model and PtyGer tool. We start with the introduction of a general parallelization design and discuss its limitations for the CG solver. We then present our hybrid parallelization model that can overcome the two challenges of CG solver parallelization.

General parallelization design

A general multi-GPU parallelization design consists of *workload distribution* and *inter-GPU communication*, which has been employed by some existing works, e.g., PtychoLib³⁸. The objectives of these two components are performing diffraction pattern distribution and sub-image border exchanges between GPUs, respectively.

Workload distribution: In ptychography, the size of the diffraction patterns d defines the workload size. Suppose that the detector is 512×512 and the number of scan positions is 16K, then d requires $512^2 \cdot 16K \cdot 4 = 16\text{GB}$ memory space. This

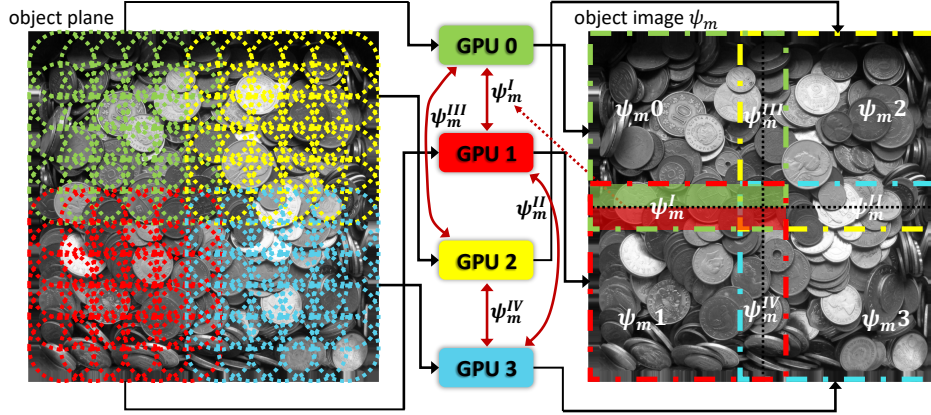


Figure 8. The basic parallelization design for a 4-GPU platform. The left-hand side of the GPUs illustrates the workload distribution while the right-hand side demonstrates the inter-GPU sub-image border exchange. Each GPU stores a portion of the diffraction patterns and locally reconstructs the corresponding sub-image. Neighbor GPUs exchange the sub-image borders after each iteration.

memory requirement, together with other data structures needed for reconstruction, can easily exceed available memory in commodity GPUs. Therefore, we partition the diffraction patterns d and distribute them to many GPUs. The left-hand side of Fig. 8 schematically demonstrates the workload distribution scheme. On the left object plane, each circle represents a scan position and has a corresponding diffraction pattern (omitted in the figure for clarity). The diffraction patterns are divided and distributed to the GPUs, then each GPU locally reconstructs the corresponding sub-image as shown on the right object image. For example, the diffraction patterns collected at green scan positions are stored in GPU 0, hence GPU 0 can locally reconstruct sub-image ψ_m^0 . Notice that to keep the sub-image borders accurate, in each GPU, we store additional diffraction patterns at the halo of the sub-image⁶⁶, and exchange the sub-image borders with neighbor GPUs after each iteration.

Inter-GPU communication: To handle the border blurring, each GPU reconstructs also the halo of the corresponding sub-image hence has overlaps with its neighbor GPUs. The right-hand side of Fig. 8 shows how the sub-images intersect with their neighbors. For each sub-image, local reconstructions only guarantee that the central area (the area within the black dotted lines) is accurate. It sub-image halos are blurred due to the missed diffraction patterns that stored in the neighbor GPUs. Therefore, the border areas of the sub-images should be exchanged between GPUs after each object-update iteration to compensate the halo blurring. For instance, GPU 0 and GPU 1 reconstruct two sub-areas enclosed by the green and red dashed squares, respectively. After each object update, the reconstructed sub-image ψ_m^0 and ψ_m^1 are accurate compared to the whole image update. However, the overlapped area ψ_m^1 is inaccurate in both GPUs. Specifically, the green area is part of ψ_m^1 's halo and is blurred in GPU 1 while the red area is blurred in GPU 0. To make the halos accurate, GPU 0 then transfers the accurate green area to GPU 1 and receives the accurate red area transferred from GPU 1.

The general parallelization of ptychography can be summarized as follows: it partitions the diffraction patterns and distributes them to different GPUs in accordance with the GPU capacity. At each iteration, GPUs locally reconstruct the corresponding sub-images with the halos, then synchronize and exchange the borders with their neighbor GPUs. After a certain number of iterations or reaching to a stop criterion, we align the locally reconstructed sub-images to obtain the entire object image.

Challenges of CG solver parallelization

Although the general parallelization is fully compatible with some reconstruction algorithms, e.g., ePIE and GD solver (Eq. (4) is directly applicable to partial reconstructions), it fails to preserve the CG solver's algorithmic equivalence due to two main challenges.

Challenge 1: In each iteration, the CG solver computes the search direction η_m using Eq. (6). Since η and $\nabla_{\psi}F(\psi)$ are matrices that have the same shape as the object image, the partial processing is compatible with the first term of Eq. (6). However, the partial processing is not directly applicable to the second term's coefficient computation.

We denote the coefficient as

$$\alpha_m = \frac{\|\nabla_{\psi}F(\psi_m)\|_2^2}{\langle \eta_{m-1}, \nabla_{\psi}F(\psi_m) - \nabla_{\psi}F(\psi_{m-1}) \rangle} \quad (8)$$

It is a scalar generated from the matrices $\nabla_{\psi}F(\psi_m)$, $\nabla_{\psi}F(\psi_{m-1})$, and η_{m-1} through norm $\|\cdot\|$ and element-wise summation. Such matrices to scalar conversion implies that Eq. (8) demands the complete data of $\nabla_{\psi}F(\psi)$ and η , and therefore it is incompatible with the local partial reconstruction in the basic parallelization design. Specifically, in the running example, the local reconstructions of the four GPUs generate four distinct scalars α_{m0} to α_{m3} based on the partial $\nabla_{\psi}F(\psi_m)_0$ to $\nabla_{\psi}F(\psi_m)_3$ and η_{m-1}_0 to η_{m-1}_3 , respectively. Neither of the four scalars can guarantee the convergence of the whole problem.

Challenge 2 Line-search stage in the CG solver is a *while loop* that dynamical determines step length. It repeatedly computes the minimization function Eq. (2) with shrunk γ_m until the condition Eq. (7) is fulfilled. In Eq. (2), d and $\mathcal{G}\psi$ at the right-hand side are 3D arrays, while $F(\psi)$ at the left-hand side is a scalar. The array to scalar conversion is performed through the element-wise summation. Such dimensional reduction implies that computing $F(\psi_m + \gamma_m\eta_m)$ demands the complete data of d and $\mathcal{G}\psi$. Therefore, similar to Eq. (8), the line-search using Eq. (7) and Eq. (2) is incompatible with the local partial reconstruction in the basic parallelization design. With the basic design, different GPUs will generate different scalar γ_m and none of them can guarantee the convergence of the whole problem.

Addressing the above challenges requires a fine-grained parallelization with additional synchronization between GPUs for the CG solver. The advanced solution needs to be compatible with both Eq. (2) and (6).

Hybrid model design

In our design, we propose a *hybrid parallelization model* for the CG solver aiming to fully maintain its algorithmic equivalence. As shown in Fig. 7, an iteration of the CG solver can be categorized to four stages. In the *GRAD stage*, the solver computes the gradient $\nabla_{\psi}F(\psi_m)$ via Eq. (3). It then computes the search direction η_m using Eq. (6) in the *DIR stage* and the step length γ_m using line-search in the *LS stage*. It finally updates the estimated object image ψ_m with Eq. (5) in the *Update stage*. The general parallelization design is applicable to the GRAD and Update stages. In order to address the two challenges described in the above subsection, we use the *gather-scatter* communication pattern for the DIR stage and the *all-reduce* pattern for the LS stage. We couple the two patterns with the basic parallelization design to construct the hybrid model.

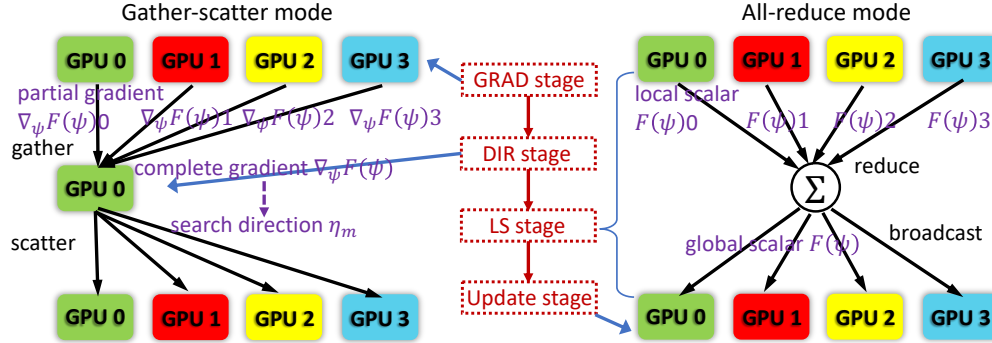


Figure 9. The schematic diagram of our hybrid parallelization model. The left drawing illustrates the workflow of gather-scatter mode while the right drawing demonstrates the workflow of all-reduce mode. The gather-scatter mode is dedicated to DIR stage. The all-reduce mode is used to repeatedly compute the minimization function for LS stage.

Fig. 9 is a schematic depicting the hybrid parallelization model. The left part of Fig. 9 demonstrates the structure and workflow of the *gather-scatter mode*, while the right part demonstrates the *all-reduce mode*'s.

Gather-scatter mode: This mode is dedicated for the DIR stage. In such mode, one GPU is selected as the *master GPU*. Without loss of generality, in the running example, GPU 0 is used as the *master GPU*. In the GRAD stage, the perspective partial gradients $\nabla_{\psi}F(\psi_m)_0$ to $\nabla_{\psi}F(\psi_m)_3$ are computed and locally stored in the corresponding GPUs. Then in the DIR stage, all local partial gradients are gathered by the master GPU 0 to form complete $\nabla_{\psi}F(\psi_m)$. The complete gradient $\nabla_{\psi}F(\psi_m)$ is a 2D matrix having the same shape of the object image ψ_m . Its data volume (usually smaller than 2048^2) is far less than the 3D array diffraction patterns d which consumes most of the memory. Therefore, the gathering overhead is lightweight. Moreover, since $\nabla_{\psi}F(\psi_{m-1})$, η_{m-1} , and $\nabla_{\psi}F(\psi_m)$ are all 2D matrices that can fit into a single GPU (GPU 0) and Eq. (6) does not rely upon 3D data d or $\mathcal{G}\psi$, the complete search direction η_m can be computed entirely in master GPU 0. Then GPU 0 splits η_m as η_{m0} to η_{m3} and scatters them to the corresponding GPUs for the next stage.

All-reduce mode: This mode is designed for the LS stage to overcome Challenge 2. As described in the previous subsection,

Eq. (2) requires the complete 3D arrays d and $\mathcal{G}\psi$. However, in contrast to the 2D array $\nabla_{\psi}F(\psi_m)$, gathering the partial d and $\mathcal{G}\psi$ into a master GPU is infeasible due to their large data volumes. On the other hand, we observe that the out-most element-wise summation in Eq. (2) converts the 3D arrays to a scalar and is the only obstacle to the local partial reconstruction. Therefore, according to the addition associativity, we can overcome Challenge 2 by summing up the partial results to get the global scalar $F(\psi_m + \gamma_m \eta_m)$. For instance, in the running example, the four GPUs compute four local scalars $F(\psi_m + \gamma_m \eta_m)_0$ to $F(\psi_m + \gamma_m \eta_m)_3$ via Eq. (2) using their perspective partial data d_0 to d_3 , $\mathcal{G}\psi_{m0}$ to $\mathcal{G}\psi_{m3}$, ψ_{m0} to ψ_{m3} , and η_{m0} to η_{m3} . The global scalar $F(\psi_m + \gamma_m \eta_m)$ then can be calculated by $\sum_{g=0}^3 F(\psi_m + \gamma_m \eta_m)_g$ and broadcast to all GPUs. Here $\sum_{g=0}^3$ serves as the generalized reduction operation.

In summary, our proposed hybrid parallelization model utilizes the gather-scatter mode to overcome Challenge 1 by avoiding the computing with partial data. It gathers the partial data into a master GPU and performs the entire DIR stage in this GPU. The computed complete search direction is then divided and scattered to the corresponding GPUs. Our hybrid model employs the all-reduce mode to overcome Challenge 2 by reducing the partial results via a summation. Summing up each GPU's partial result preserves the algorithmic equivalence to Eq. (2). The summed scalar $F(\psi_m + \gamma_m \eta_m)$ is then broadcast to all GPUs. The LS stage keeps iterating by shrinking the step length γ_m and computing $F(\psi_m + \gamma_m \eta_m)$ in all-reduce mode until Eq. (7) is fulfilled. The hybrid model then switches back to the basic parallelization design and updates the object image ψ_m accordingly.

PtyGer Implementation

We implement the proposed hybrid parallelization model in PtyGer, which is a high-performance multi-GPU based tool for the ptychographic reconstruction. To conform to the computational imaging domain's preference, PtyGer is written in Python using CuPy (<https://cupy.chainer.org/>) library. Alg. 1 demonstrates the complete workflow of PtyGer. After partitioning and copying the inputs from the host to the GPU devices (Line 4), PtyGer iteratively updates the object image until the number of iteration reaches the limit (Line 6-26). In each iteration, PtyGer first locally computes the partial gradients in corresponding GPUs during the GRAD stage (Line 8-9), then switches to the gather-scatter mode to calculate the search-direction in the DIR stage (Line 10-14). It subsequently switches to the all-reduce mode and determines the step-length via the line-search (Line 15-23). During the line-search, it repeatedly executes the minimization function (Line 19-22) until the stop condition is satisfied (Line 23). PtyGer finally updates the subimages in every GPUs (Line 25) and exchanges their borders (Line 26). At the end of iterative updates, all subimages are transferred from GPUs to CPU and aligned to form the complete object image (Line 27). PtyGer is open source and available at GitHub (<https://github.com/xiaodong-yu/PtyGer>).

References

1. Abbey, B. *et al.* Keyhole coherent diffractive imaging. *Nat. Phys.* **4**, 394–398 (2008).
2. Dierolf, M. *et al.* Ptychography & lensless x-ray imaging. *Europhys. News* **39**, 22–24 (2008).
3. Chapman, H. N. & Nugent, K. A. Coherent lensless x-ray imaging. *Nat. Photonics* **4**, 833 (2010).
4. Nugent, K. A. Coherent methods in the x-ray sciences. *Adv. Phys.* **59**, 1–999 (2010).
5. Miao, J., Sandberg, R. L. & Song, C. Coherent x-ray diffraction imaging. *IEEE J. Sel. Top. Quantum Electron.* **18**, 399–410 (2012).
6. Miao, J., Ishikawa, T., Robinson, I. K. & Murnane, M. M. Beyond crystallography: Diffractive imaging using coherent x-ray light sources. *Science* **348**, 530–535 (2015).
7. Hoppe, W. Beugung im inhomogenen Primärstrahlwellenfeld, I: Prinzip einer Phasenmessung. *Acta Crystallogr. A* **25**, 495–501 (1969).
8. Pfeiffer, F. X-ray ptychography. *Nat. Photonics* **12**, 9–17 (2018).
9. Aslan, S. *et al.* Joint ptycho-tomography reconstruction through alternating direction method of multipliers. *Opt. express* **27**, 9128–9143 (2019).
10. Ching, D. J., Hidayetoğlu, M., Biçer, T. & Gürsoy, D. Rotation-as-fast-axis scanning-probe x-ray tomography: the importance of angular diversity for fly-scan modes. *Appl. optics* **57**, 8780–8789 (2018).
11. Faulkner, H. & Rodenburg, J. Movable aperture lensless transmission microscopy: a novel phase retrieval algorithm. *Phys. Rev. Lett.* **93**, 023903 (2004).
12. Rodenburg, J. M. & Faulkner, H. M. L. A phase retrieval algorithm for shifting illumination. *Appl. Phys. Lett.* **85**, 4795–4797 (2004).

Algorithm 1: Complete workflow of PtyGer

```
1 Input: complex64  $h_\psi, h_p$ ; float32  $h_s, h_d$ ;  
2 Spawn T threads, T = Number of GPUs  
   /* partition and distribute the workloads in the CPU host to different GPU devices */  
3 in thread $_i, i \in \text{GPU\_ids}$ : with GPU device  $i$  do                                ▷ each thread is assigned a GPU device  
4   |  $d_\psi_{0i} \leftarrow h_\psi, d_p \leftarrow h_p, d_s \leftarrow h_s, d_d \leftarrow h_d$ ;    ▷ copy data from host ( $h_*$ ) to device ( $d_*$ )  
5    $m = 0$ ;  
6 while  $m < \text{iter\_limit}$  do  
7   in thread $_i, i \in \text{GPU\_ids}$ : with GPU device  $i$  do  
8     /* GRAD stage */  
9      $\mathcal{G} \psi_i = \text{FORWARD}(d_\psi_{mi}, d_p, d_s)$ ;  
10     $\nabla_\psi F(\psi)_i = \text{GRAD\_COMP}(\mathcal{G} \psi_i, d_d)$ ;  
11    /* DIR stage; switch to the gather-scatter mode */                                ▷ locally compute the partial gradient via Eq.(5)  
12     $\nabla_\psi F(\psi) \leftarrow \nabla_\psi F(\psi)_0 \cup \nabla_\psi F(\psi)_i$ ;  
13    thread_sync;                                                                    ▷ copy the partial gradient to master GPU 0 (gather)  
14    in thread $_0$ : with GPU device 0 do  
15       $\eta = \text{DAI-YUAN}(\nabla_\psi F(\psi))$ ;  
16       $\eta \rightarrow \eta_i$ ;  
17    /* LS stage; switch to the all-reduce mode */                                    ▷ compute the complete search direction in master GPU 0 via Eq.(7)  
18     $\gamma^{(0)} = 1; \tau = 0.5; k = 0$ ;  
19    do                                                                              ▷ split and distribute the search direction to slave GPUs (scatter)  
20      in thread $_i, i \in \text{GPU\_ids}$ : with GPU device  $i$  do  
21         $\gamma^{(k+1)} \leftarrow \gamma^{(k)} \tau$ ;  
22         $\mathcal{G}(\psi + \gamma^{(k)} \eta)_i = \text{FORWARD}(d_\psi_{mi} + \gamma^{(k)} \eta_i, d_p, d_s)$ ;  
23         $F(\psi + \gamma^{(k)} \eta)_i = \text{MINFUNC}(\mathcal{G}(\psi + \gamma^{(k)} \eta)_i, d_d)$ ;  
24        thread_sync;                                                                    ▷ locally compute the result via Eq.(4)  
25         $F(\psi + \gamma^{(k)} \eta) \leftarrow \sum F(\psi + \gamma^{(k)} \eta)_i$ ;  
26        /* Update stage; switch back to the basic design */                          ▷ sum up the partial results then broadcast it (all-reduce)  
27        while  $F(\psi + \gamma^{(k)} \eta) \leq F(\psi_m) + \gamma^{(k)} t$ ;  
28        in thread $_i, i \in \text{GPU\_ids}$ : with GPU device  $i$  do  
29           $d_\psi_{(m+1)i} \leftarrow d_\psi_{mi} + \gamma^{(k)} \eta_i$ ;  
30          exchange the border of  $d_\psi_{mi}$   
31 Output:  $h_\psi \leftarrow \cup d_\psi_{mi}$                                                     ▷ copy the partial images back to host and unite them
```

13. Maiden, A. M. & Rodenburg, J. M. An improved ptychographical phase retrieval algorithm for diffractive imaging. *Ultramicroscopy* **109**, 1256–1262 (2009).
14. Thibault, P. *et al.* High-resolution scanning x-ray diffraction microscopy. *Science* **321**, 379–382 (2008).
15. Thibault, P., Dierolf, M., Bunk, O., Menzel, A. & Pfeiffer, F. Probe retrieval in ptychographic coherent diffractive imaging. *Ultramicroscopy* **109**, 338–343 (2009).
16. Guizar-Sicairos, M. & Fienup, J. R. Phase retrieval with transverse translation diversity: a nonlinear optimization approach. *Opt. express* **16**, 7264–7278 (2008).
17. Thibault, P. & Guizar-Sicairos, M. Maximum-likelihood refinement for coherent diffractive imaging. *New J. Phys.* **14**, 063004 (2012).
18. Odstrčil, M., Menzel, A. & Guizar-Sicairos, M. Iterative least-squares solver for generalized maximum-likelihood ptychography. *Opt. express* **26**, 3108–3123 (2018).
19. Dong, Z. *et al.* High-performance multi-mode ptychography reconstruction on distributed GPUs. *arXiv preprint arXiv:1808.10375* (2018).
20. Yu, X. & Becchi, M. Exploring different automata representations for efficient regular expression matching on GPUs. *ACM SIGPLAN Notices* **48**, 287–288 (2013).
21. Yu, X. & Becchi, M. GPU acceleration of regular expression matching for large datasets: Exploring the implementation space. In *Proceedings of the ACM International Conference on Computing Frontiers*, CF '13, 18:1–18:10, DOI: [10.1145/2482767.2482791](https://doi.org/10.1145/2482767.2482791) (ACM, New York, NY, USA, 2013).

22. Nourian, M., Wang, X., Yu, X., Feng, W.-c. & Becchi, M. Demystifying automata processing: GPUs, FPGAs or micron's AP? In *Proceedings of the International Conference on Supercomputing, ICS '17* (ACM, 2017).
23. Yu, X. *Deep packet inspection on large datasets: algorithmic and parallelization techniques for accelerating regular expression matching on many-core processors* (University of Missouri-Columbia, 2013).
24. Hou, K., Wang, H. & Feng, W.-c. Aalign: A SIMD framework for pairwise sequence alignment on x86-based multi-and many-core processors. In *2016 IEEE International Parallel and Distributed Processing Symposium (IPDPS)*, 780–789 (IEEE, 2016).
25. Zhang, J., Wang, H. & Feng, W.-c. cublastp: Fine-grained parallelization of protein sequence search on CPU+GPU. *IEEE/ACM Transactions on Comput. Biol. Bioinforma. (TCBB)* **14**, 830–843 (2017).
26. Yu, X. *et al.* GPU-based static data-flow analysis for fast and scalable android app vetting. In *The 34th IEEE International Parallel and Distributed Processing Symposium (IPDPS)* (IEEE, 2020).
27. Yu, X. *Algorithms and Frameworks for Accelerating Security Applications on HPC Platforms*. Ph.D. thesis, Virginia Tech (2019).
28. Yu, X., Wang, H., Feng, W.-c., Gong, H. & Cao, G. cuART: fine-grained algebraic reconstruction technique for computed tomography images on GPUs. In *2016 16th IEEE/ACM International Symposium on Cluster, Cloud and Grid Computing (CCGrid)*, 165–168 (IEEE, 2016).
29. Gürsoy, D., De Carlo, F., Xiao, X. & Jacobsen, C. TomoPy: a framework for the analysis of synchrotron tomographic data. *J. synchrotron radiation* **21**, 1188–1193 (2014).
30. Yu, X., Wang, H., Feng, W.-c., Gong, H. & Cao, G. An enhanced image reconstruction tool for computed tomography on GPUs. In *Proceedings of the Computing Frontiers Conference, CF'17*, 97–106 (ACM, 2017).
31. Hidayetoğlu, M. *et al.* Memxct: Memory-centric x-ray CT reconstruction with massive parallelization. In *Proceedings of the International Conference for High Performance Computing, Networking, Storage and Analysis*, 1–56 (2019).
32. Yu, X., Wang, H., Feng, W.-c., Gong, H. & Cao, G. GPU-based iterative medical CT image reconstructions. *J. Signal Process. Syst.* **91**, 321–338 (2019).
33. Nikitin, V. *et al.* Photon-limited ptychography of 3D objects via Bayesian reconstruction. *OSA Continuum* **2**, 2948–2968 (2019).
34. Wakonig, K. *et al.* PtychoShelves, a versatile high-level framework for high-performance analysis of ptychographic data. *J. Appl. Crystallogr.* **53** (2020).
35. Hines, J. Stepping up to summit. *Comput. science & engineering* **20**, 78–82 (2018).
36. Papka, M. E., Collins, J., Cerny, B. & Heinonen, N. 2018 annual report-argonne leadership computing facility. Tech. Rep., Argonne National Lab.(ANL), Argonne, IL (United States) (2018).
37. Gayatri, R., Gott, K. & Deslippe, J. Comparing managed memory and ats with and without prefetching on nvidia volta gpus. In *2019 IEEE/ACM Performance Modeling, Benchmarking and Simulation of High Performance Computer Systems (PMBS)*, 41–46 (IEEE, 2019).
38. Nashed, Y. S. *et al.* Parallel ptychographic reconstruction. *Opt. express* **22**, 32082–32097 (2014).
39. Marchesini, S. *et al.* SHARP: a distributed GPU-based ptychographic solver. *J. applied crystallography* **49**, 1245–1252 (2016).
40. Luke, D. R. Relaxed averaged alternating reflections for diffraction imaging. *Inverse problems* **21**, 37 (2004).
41. Thakur, R., Rabenseifner, R. & Gropp, W. Optimization of collective communication operations in mpich. *The Int. J. High Perform. Comput. Appl.* **19**, 49–66 (2005).
42. Wang, H., Potluri, S., Bureddy, D., Rosales, C. & Panda, D. K. Gpu-aware mpi on rdma-enabled clusters: Design, implementation and evaluation. *IEEE Transactions on Parallel Distributed Syst.* **25**, 2595–2605 (2013).
43. Awan, A. A., Hamidouche, K., Hashmi, J. M. & Panda, D. K. S-caffe: Co-designing mpi runtimes and caffe for scalable deep learning on modern gpu clusters. In *Proceedings of the 22nd ACM SIGPLAN Symposium on Principles and Practice of Parallel Programming*, 193–205 (2017).
44. Awan, A. A., Bédorf, J., Chu, C.-H., Subramoni, H. & Panda, D. K. Scalable distributed dnn training using tensorflow and cuda-aware mpi: Characterization, designs, and performance evaluation. In *2019 19th IEEE/ACM International Symposium on Cluster, Cloud and Grid Computing (CCGRID)*, 498–507 (IEEE, 2019).

45. NVIDIA. *NVIDIA Collective Communication Library (NCCL) Documentation*. ((accessed Oct. 20, 2020)). <https://docs.nvidia.com/deeplearning/nccl/user-guide/docs/>.
46. Enfedaque, P., Chang, H., Enders, B., Shapiro, D. & Marchesini, S. High performance partial coherent x-ray ptychography. In *International Conference on Computational Science*, 46–59 (Springer, 2019).
47. Rodenburg, J., Hurst, A. & Cullis, A. Transmission microscopy without lenses for objects of unlimited size. *Ultramicroscopy* **107**, 227–231 (2007).
48. Rodenburg, J. *et al.* Hard-x-ray lensless imaging of extended objects. *Phys. review letters* **98**, 034801 (2007).
49. Maiden, A., Johnson, D. & Li, P. Further improvements to the ptychographical iterative engine. *Optica* **4**, 736–745 (2017).
50. Maiden, A. M., Humphry, M. J. & Rodenburg, J. Ptychographic transmission microscopy in three dimensions using a multi-slice approach. *JOSA A* **29**, 1606–1614 (2012).
51. Enders, B. & Thibault, P. A computational framework for ptychographic reconstructions. *Proc. Royal Soc. A: Math. Phys. Eng. Sci.* **472**, 20160640 (2016).
52. Deng, J. *et al.* The velociprobe: An ultrafast hard x-ray nanoprobe for high-resolution ptychographic imaging. *Rev. Sci. Instruments* **90**, 083701 (2019).
53. Mandula, O., Elzo Aizarna, M., Eymery, J., Burghammer, M. & Favre-Nicolin, V. PyNX. Ptycho: a computing library for X-ray coherent diffraction imaging of nanostructures. *J. Appl. Crystallogr.* **49**, 1842–1848 (2016).
54. Wang, L., Wu, W., Xu, Z., Xiao, J. & Yang, Y. Blasx: A high performance level-3 BLAS library for heterogeneous multi-GPU computing. In *Proceedings of the 2016 International Conference on Supercomputing*, 1–11 (2016).
55. Pan, Y., Wang, Y., Wu, Y., Yang, C. & Owens, J. D. Multi-GPU graph analytics. In *2017 IEEE International Parallel and Distributed Processing Symposium (IPDPS)*, 479–490 (IEEE, 2017).
56. Ben-Nun, T., Sutton, M., Pai, S. & Pingali, K. Groute: An asynchronous multi-GPU programming model for irregular computations. *ACM SIGPLAN Notices* **52**, 235–248 (2017).
57. Ben-Nun, T., Levy, E., Barak, A. & Rubin, E. Memory access patterns: the missing piece of the multi-GPU puzzle. In *SC'15: Proceedings of the International Conference for High Performance Computing, Networking, Storage and Analysis*, 1–12 (IEEE, 2015).
58. Wang, G. *et al.* Blink: Fast and generic collectives for distributed ML. *arXiv preprint arXiv:1910.04940* (2019).
59. Wang, Z., Bovik, A. C., Sheikh, H. R. & Simoncelli, E. P. Image quality assessment: from error visibility to structural similarity. *IEEE transactions on image processing* **13**, 600–612 (2004).
60. Reiffen, B. & Sherman, H. An optimum demodulator for poisson processes: Photon source detectors. *Proc. IEEE* **51**, 1316–1320 (1963).
61. Dai, Y. H. & Yuan, Y. A nonlinear conjugate gradient method with a strong global convergence property. *SIAM J. Optim.* **10**, 177–182 (1999).
62. Dai, Y. *et al.* Convergence properties of nonlinear conjugate gradient methods. *SIAM J. on Optim.* **10**, 345–358 (2000).
63. Polak, E. & Ribiere, G. Note sur la convergence de méthodes de directions conjuguées. *ESAIM: Math. Model. Numer. Analysis-Modélisation Mathématique et Analyse Numérique* **3**, 35–43 (1969).
64. Polyak, B. T. The conjugate gradient method in extremal problems. *USSR Comput. Math. Math. Phys.* **9**, 94–112 (1969).
65. Nocedal, J. & Wright, S. *Numerical optimization* (Springer Science & Business Media, 2006).
66. Guizar-Sicairos, M. *et al.* High-throughput ptychography using eiger: scanning x-ray nano-imaging of extended regions. *Opt. express* **22**, 14859–14870 (2014).

Acknowledgements (not compulsory)

This material is based upon work supported by the U.S. Department of Energy, Office of Science, Basic Energy Sciences and Advanced Scientific Computing Research, under Contract DE-AC02-06CH11357. This research used resources of the Advanced Photon Source, a U.S. Department of Energy (DOE) Office of Science User Facility operated for the DOE Office of Science by Argonne National Laboratory under the same contract. Authors acknowledge Junjing Deng, Yudong Yao, Yi Jiang, Jeffrey Klug, Nick Sirica, and Jeff Nguyen for providing the experimental data acquired on the Velociprobe instrument at beamline 2-ID-D of the Advanced Photon Source, Argonne National Laboratory. This work was performed, in part, at the Center for Integrated Nanotechnologies, an Office of Science User Facility operated for the U.S. Department of Energy

(DOE) Office of Science. Los Alamos National Laboratory, an affirmative action equal opportunity employer, is managed by Triad National Security, LLC for the U.S. Department of Energy's NNSA, under contract 89233218CNA000001. This work is partially supported by the Office of the Director of National Intelligence (ODNI), Intelligence Advanced Research Projects Activity (IARPA), via contract D2019-1903270004. The views and conclusions contained herein are those of the authors and should not be interpreted as necessarily representing the official policies or endorsements, either expressed or implied, of the ODNI, IARPA, or the U.S. Government.

Author contributions statement

Must include all authors, identified by initials, for example: A.A. conceived the experiment(s), A.A. and B.A. conducted the experiment(s), C.A. and D.A. analysed the results. All authors reviewed the manuscript.

Additional information

To include, in this order: **Accession codes** (where applicable); **Competing interests** (mandatory statement).

The corresponding author is responsible for submitting a [competing interests statement](#) on behalf of all authors of the paper. This statement must be included in the submitted article file.